

QUaRTM: A Quadcopter with Unactuated Rotor Tilting Mechanism Capable of Faster, More Agile, and More Efficient Flight

Jerry Tang, Karan P. Jain, and Mark W. Mueller

Authors are with the High Performance Robotics Lab, Department of Mechanical Engineering, University of California Berkeley, USA

Correspondence*:
Corresponding Author
jerrytang@berkeley.edu

2 ABSTRACT

3 We present QUaRTM – a novel quadcopter design capable of tilting the propellers into the
4 forward flight direction, which reduces the drag area and therefore allows for faster, more agile,
5 and more efficient flight. The vehicle can morph between two configurations in mid-air, including
6 the untilted configuration and the tilted configuration. The vehicle in the untilted configuration
7 has a higher pitch torque capacity and a smaller vertical dimension. The vehicle in the tilted
8 configuration has a lower drag area, leading to a higher top speed, higher agility at high speed,
9 and better flight efficiency. The morphing is accomplished without any additional actuators beyond
10 the four motors of a quadcopter. The rigid connections between the quadcopter frame and the
11 quadcopter arms are replaced with sprung hinges. This allows the propellers to be tilted when
12 high thrusts are produced, and recover to the untilted configuration when the thrusts are brought
13 low. The effectiveness of such a vehicle is demonstrated by running experiments on a prototype
14 vehicle with a shape similar to a regular quadcopter. Through the use of tilting, the vehicle is
15 shown to have a 12.5% higher maximum speed, better high-speed agility as the maximum crash-
16 free cruise speed increased by 7.5%, and a better flight efficiency as the power consumption has
17 dropped by more than 20% in the speed range of 15-20m s⁻¹.

18 **Keywords:** Morphing quadcopter, Agile, Efficient, High-speed, Mechanism design, Aerodynamics

1 INTRODUCTION

19 Over the past decade, UAVs have become increasingly popular. One of the most common UAV designs
20 is the quadcopter which is a multirotor device driven by four independently controlled propellers. The
21 simplicity and agility of quadcopters as explained in (Mueller et al., 2022) have made them one of the
22 preferred choices for a variety of applications, such as surveillance (Jaimes et al., 2008), mapping (Siebert
23 and Teizer, 2014), building inspection, photography, delivery (Thiels et al., 2015), and disaster management
24 (Erdelj et al., 2017). Nevertheless, conventional quadcopters are usually not able to achieve a high top
25 speed, nor are they able to fly efficiently at a high speed. This is related to the fact that a quadcopter has
26 to tilt its body toward the forward flight direction to counter the drag. However, tilting the quadcopter
27 body means that a larger area is now subject to air resistance, which in turn increases the burden on the
28 propellers. In addition to limiting the top speed, this also reduces the flight efficiency and might cause

29 the quadcopter to stall. For tasks such as search and rescue and rapid package delivery that are both time
30 and cost sensitive, and still require the vehicle to have high agility and vertical take-off capacity, we see
31 a demand for a quadcopter platform that is capable of efficient high-speed flight (Frachtenberg, 2019;
32 Poikonen and Campbell, 2020).

33 Some work has been done on increasing the flight efficiency and endurance of quadcopters. A method
34 for finding the optimal speed and sideslip angle of a multicopter was presented in Wu et al. (2022). An
35 approach to extending endurance and range by docking secondary quadcopters carrying replacement
36 batteries is shown in Jain et al. (2020a). An increase in flight time by using the battery in multiple stages has
37 been demonstrated in Jain et al. (2020b). Solar-powered UAVs, which can potentially fly large distances,
38 have been explored in Reinhardt et al. (1996).

39 Since the limit on the top speed of a conventional quadcopter often has to do with its inherent aerodynamic
40 properties, a more fundamental design change is often required to improve the efficiency and flight speed.
41 A common design that can achieve the said goals is the tilt-rotor design. A tilt-rotor allows the propellers
42 to be tilted toward the flight direction without the need for tilting the main body, thereby reducing the area
43 subject to wind. Several tilt-rotor quadcopter designs have been explored. A convertible prototype "Quad
44 Tilt Rotor" capable of vertical takeoffs like a quadcopter, and high-speed flight like a fixed-wing UAV was
45 presented in Lin et al. (2014). A control scheme to handle the flight mode conversion from a helicopter to
46 a fixed-wing "Quad-TiltRotors" was presented in Papachristos et al. (2013). A constrained robust model
47 reference adaptive controller of an H-shaped tilt-rotor was presented in Anderson et al. (2021). In addition
48 to fusing a fixed-wing and a conventional quadcopter to enable the vehicle to travel at a high speed, several
49 other tilt rotors designs have been explored. A tilt-rotor quadcopter capable of achieving any arbitrary
50 desired state or configuration by tilting each rotor independently was presented in Nemati et al. (2016).
51 The design and optimal control of an omnidirectional micro aerial vehicle capable of exerting a wrench in
52 any orientation while maintaining efficient flight configurations were presented in Allenspach et al. (2020).



Figure 1. The experimental vehicle hovering in the untilted (left) and tilted (right) configurations.

53 We propose a novel tilt-rotor vehicle design – a quadcopter with an unactuated rotor tilting mechanism
54 (QUaRTM), capable of tilting the propellers into the forward flight direction without the use of any actuators
55 beyond the four quadcopter motors. QUaRTM has two configurations: the untilted configuration with
56 all propeller planes parallel to the central body, and the tilted configuration with all rotors tilted into the
57 forward flight direction by an angle of 20 degrees. A photo of QUaRTM hovering in both configurations is
58 shown in Figure 1. In contrast to a conventional quadcopter, the rigid connections between the quadcopter
59 arms and the central body are replaced with hinges. This allows the propellers to tilt into the forward

60 flight direction without having to tilt the central body. Springs are added at the hinges to pull the arms into
 61 the untilted configuration. When the net propeller thrust is high enough to overcome the torque from the
 62 springs, the vehicle will transition into the tilted configuration. Then from the tilted configuration, when
 63 the net propeller thrust drops below a threshold, the arms will untilt and restore the vehicle to the untilted
 64 configuration. The spring torque acting on the arm is high in the untilted configuration and low in the tilted
 65 configuration. This creates a mechanical hysteresis that 1. prevents oscillations in the tilting behavior, 2.
 66 avoids unintended tilting or untilting, and 3. allows the propellers to produce a wider range of thrusts in
 67 both configurations. Figure 2 shows the internal architecture of the tilting mechanism.

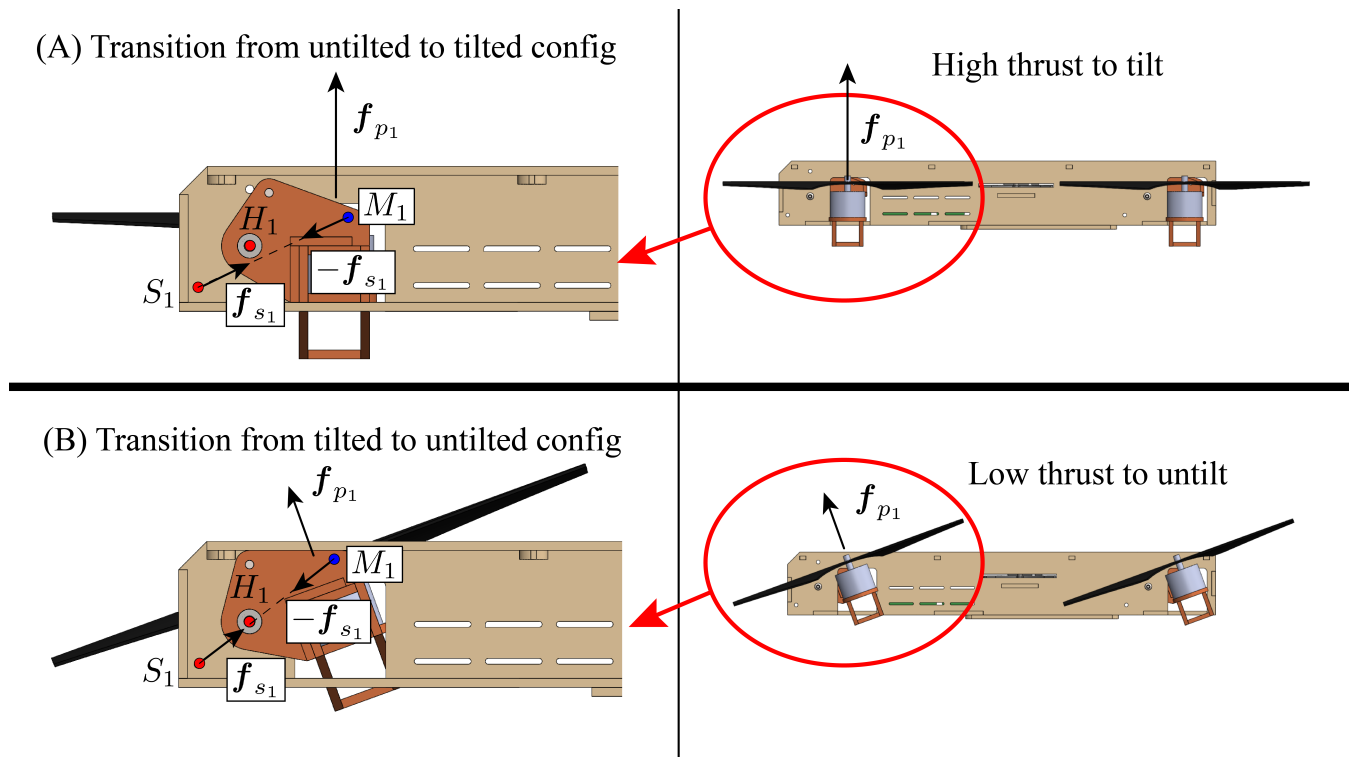


Figure 2. The vehicle viewing from the left side and the internal tilting mechanism for the front-right arm. The fuselage is shown in beige. The arm shown in red orange is allowed to rotate around hinge H_1 . A spring is attached between point S_1 on the quadcopter central body and M_1 on the arm. The spring produces a torque on the arm around hinge H_1 that tries to keep the arm in the untilted configuration. The tensions in the spring are very close for the two configurations because the amount of extension is nearly identical. However, in the untilted configuration, the distance from hinge H_1 to line S_1M_1 is large, leading to a large moment arm and a large torque produced by the spring. Thus the arm will only tilt when a very high thrust is produced, allowing the vehicle in the untilted configuration to operate at a high maximum thrust. Once the spring torque is overcome by producing a high thrust, the arm will tilt and the torque exerted by the spring will reduce because the moment arm has reduced. This ensures that the arm will not untilt so easily, allowing the vehicle in the tilted configuration to operate at a low minimum thrust.

68 QUaRTM thus combines both the advantages of flying in the untilted configuration and flying in the
 69 tilted configuration with some trade-offs. When flying in the untilted configuration, the offset between
 70 the front and rear rotors' thrust axes is the largest, resulting in the highest pitch torque capacity at lower
 71 speed. In addition, since the propellers' plane is parallel to the quadcopter frame's top plane, the vertical
 72 dimension of the vehicle is small, which makes it theoretically possible for the vehicle to fly through
 73 narrower gaps. When flying in the tilted configuration, since the central body is not tilted toward the

74 forward flight direction, the drag reflected on the vehicle is low. This allows the vehicle to achieve a higher
 75 top speed and a higher energy efficiency. In addition, the reduction in drag allows a greater portion of the
 76 vehicle's thrust capacity to be used for maneuvering instead of merely countering drag. This improves the
 77 high-speed agility of the vehicle. On the other hand, this vehicle has a slightly reduced range of thrust and
 78 torques. This is because to prevent unintended tilting and untilting, additional thrust constraints on the
 79 propellers need to be imposed. In addition, there is a slight increase in the mass and mechanical complexity
 80 of the vehicle due to the addition of the tilting mechanism.

81 Therefore, we argue that the proposed design is advantageous to existing solutions where the quadcopter is
 82 primarily expected to take off and land vertically, and fly at a high speed with high agility. Such applications
 83 are common when the targets are time-sensitive, e.g. long-distance package delivery, drone racing, search
 84 and rescue. This paper will discuss the dynamics of the QUaRTM, the principles that govern the design
 85 of the vehicle, the experimental vehicle and its controller, and the experiments conducted to validate the
 86 design and its capabilities, including 1. the mid-air tilting and untilting transitions, 2. the improvements on
 87 the maximum vehicle speed and high-speed agility, and 3. the improvements on flight efficiency when the
 88 vehicle travels at a high speed.

2 SYSTEM OVERVIEW

89 In this section, we will provide an overview of the system. We will define the model of the vehicle and
 90 derive its dynamics. This will help us to 1. find the constraints on the propeller thrusts to prevent unintended
 91 tilting and untilting, and 2. design for the vehicle frame and the tilt angle.

92 2.1 Notation

93 We follow the notations in (Bucki and Mueller, 2019) for defining the model of the vehicle. Non-bold
 94 symbols like m represent scalars, lowercase bold symbols like \mathbf{g} represent vectors, and uppercase bold
 95 symbols like \mathbf{J} represent matrices. Subscripts such as m_C represent the body to which the symbol refers,
 96 and superscripts such as \mathbf{g}^E represent the frame in which the vector is expressed. A second subscript
 97 or superscript such as ω_{CE} or \mathbf{R}^{CE} represents what the quantity is defined with respect to. However,
 98 the special superscript T represents the transpose of a matrix. To express a cross product, we use the
 99 skew-symmetric matrix form such that $\mathbf{a} \times \mathbf{b} = \mathbf{S}(\mathbf{a})\mathbf{b}$. The symbol \mathbf{d} represents a displacement, ω
 100 represents an angular velocity, and \mathbf{R} represents a rotational matrix.

101 2.2 Model

102 First of all, we define a model of the vehicle which we will use for analysis. Figure 3 shows the quadcopter
 103 model as seen from the top. We model the system as 5 coupled rigid bodies, including the central body of
 104 the quadcopter and the 4 quadcopter arms with the rotors mounted. We denote the Earth frame as E , the
 105 central body frame as C , and the frame for each arm as A_i for $i \in \{1, 2, 3, 4\}$. The origin of any frame
 106 is defined to be at the center of mass of the corresponding body. For the central body frame, the x-axis
 107 x_C points to the front of the vehicle, and the z-axis z_C points upward from the body's top surface. The
 108 rotation matrix of central body frame C with respect to the Earth frame E is defined as \mathbf{R}^{CE} . For a vector
 109 expressed in the Earth frame \mathbf{v}^E , $\mathbf{v}^C = \mathbf{R}^{CE}\mathbf{v}^E$ represents its expression in the central body frame.

110 Each arm is allowed to tilt with respect to the central body frame C around the \mathbf{y}_C direction, and the fully
 111 tilted tilt angle is defined as β . Throughout this paper, we will assume that all arms tilt at the same angle.
 112 We also define the combined arm frame A which has axes aligned with any arm i , and its origin located at

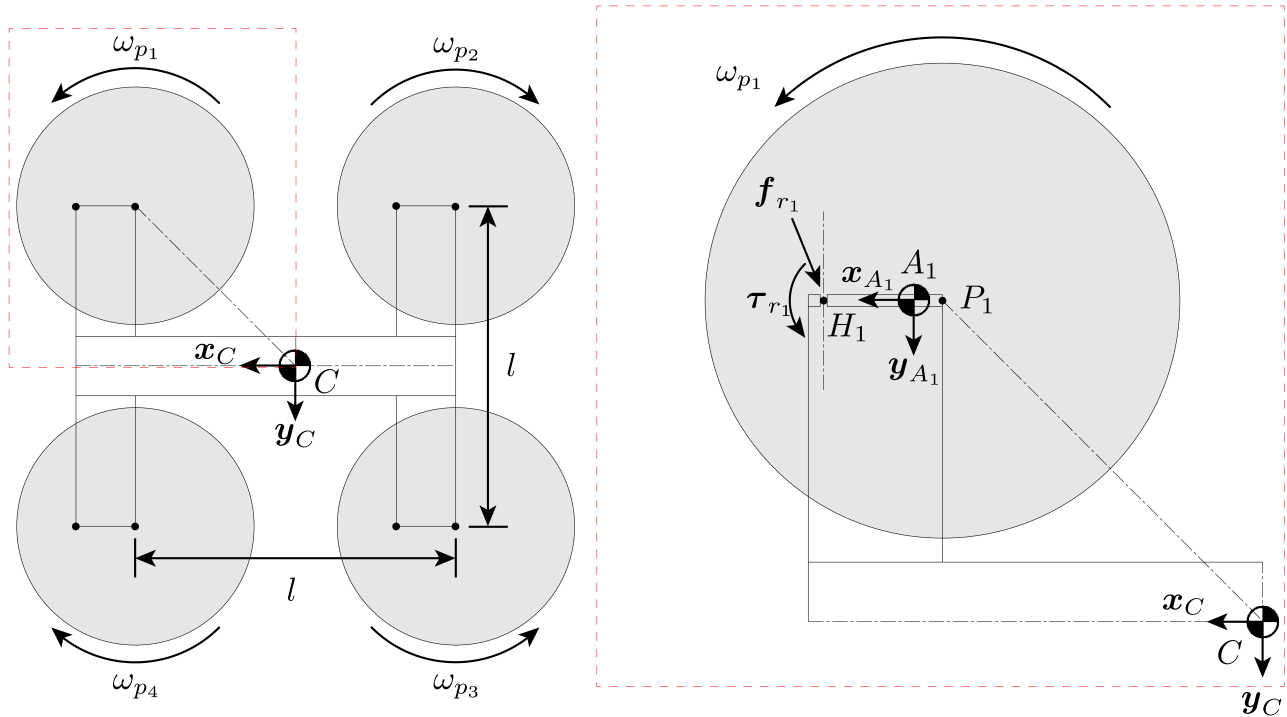


Figure 3. Top-down view of the vehicle model in the untilted configuration. The propellers are numbered 1, 2, 3, 4 in a clockwise manner. The right side shows the detailed view of rotor 1, where P_1 is the location of the rotor, A_1 is the COM of the arm that the rotor is attached to, and H_1 is the hinge that the arm can tilt about. Reaction force f_{r_1} and torque τ_{r_1} act in opposite directions between each arm and the central body at the hinge H_1 .

113 the center of mass of the whole vehicle. When an arm is not tilted, all 3 axes point in the same directions as
 114 those of the central body frame, that $x_C = x_{A_i}, y_C = y_{A_i}, z_C = z_{A_i}$. Since tilting only happens in the
 115 $y_C = y_{A_i}$ direction, only z_{A_i} and x_{A_i} will change when the arm tilts. The rotation matrix of an arm with
 116 respect to the central body is thus a single degree of freedom rotation matrix defined as $R^{A_i C}$.

117 Figure 4 shows forces and torques acting on arm 1. Note that while the figure shows only arm 1, the
 118 model can be generalized to all arms. To control the thrust at which the arm will tilt or untilt, a spring
 119 producing a force f_{s_i} is connected between point S_i on the central body and point M_i on arm i . Note
 120 that spring is not the only option here but rather a design choice. Other widgets like magnets can be also
 121 used to produce such force. In addition to the spring force and the total acceleration force, arm i also sees
 122 the propeller force and torque ($f_{p_i} = f_{p_i} z_{p_i}, \tau_{p_i} = \tau_{p_i} z_{p_i}$), and the hinge's reaction force and torque
 123 ($-f_{r_i}, -\tau_{r_i}$). The mass and moment of inertia of the central body at its center of mass are denoted as
 124 m_C and J_C respectively. Similarly, the mass and moment of inertia of any arm i at its center of mass are
 125 denoted as m_A and J_A .

126 2.3 Aerodynamics

127 Now, we model the aerodynamics of the vehicle. We will use these results to design for the tilt angle
 128 in Section 3.3. We express the aerodynamics of the quadcopter in the Earth frame E . Assuming that the
 129 quadcopter is cruising in the x_E direction at a fixed height, the drag and lift forces are:

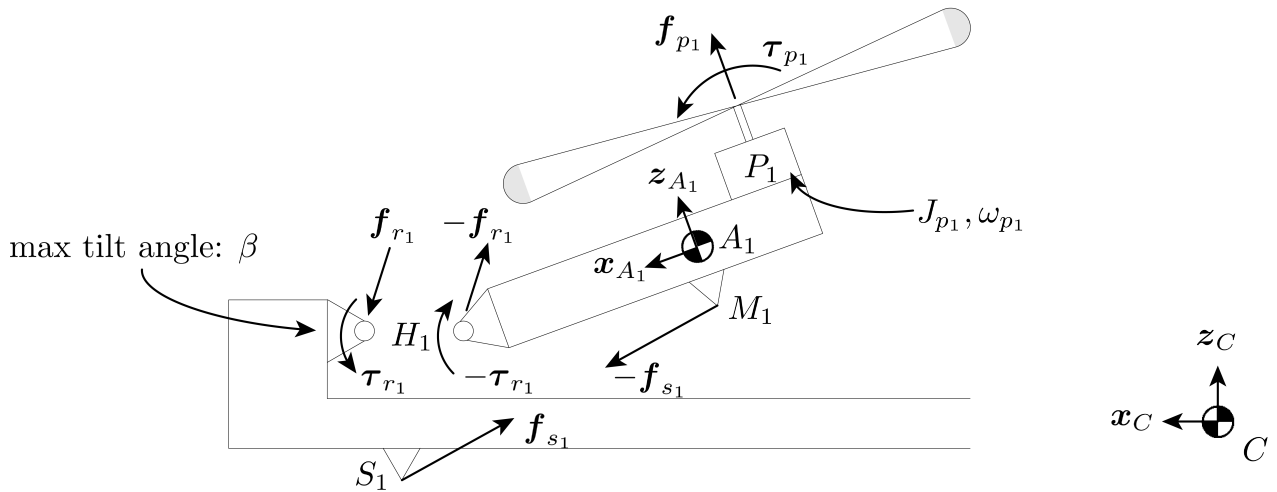


Figure 4. Free-body diagram showing the forces acting on arm 1 viewing from the left side. The length of the arm is exaggerated. A spring is attached between point S_1 on the quadcopter central body and M_1 on the arm. The spring exerts a torque that tries to keep the arm in the untilted configuration. The propeller produces a thrust force f_{p_i} and a torque τ_{p_i} in the z_{A_1} direction. The momentum of inertia of the rotor around its axis is J_{p_1} , and the rotor rotates at a speed of ω_{p_1} .

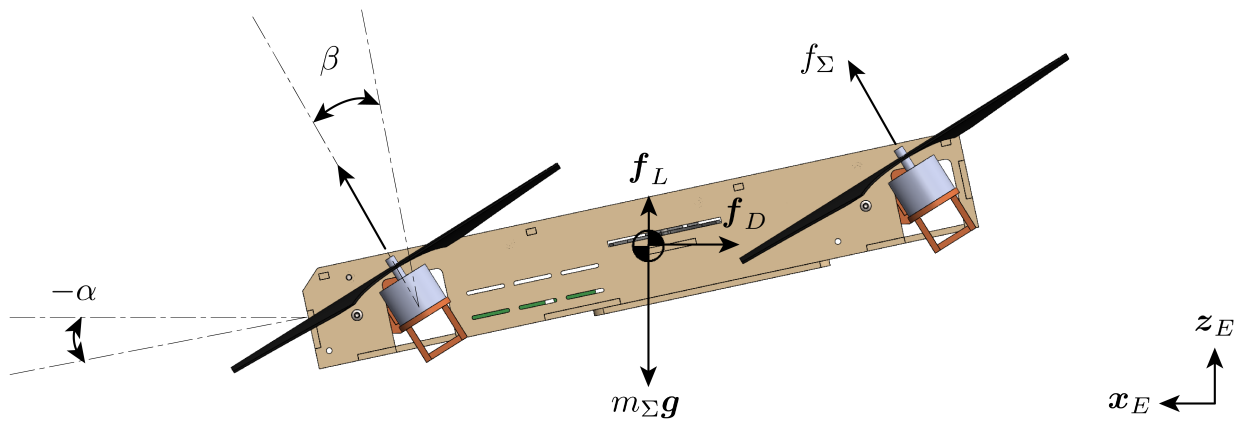


Figure 5. Free-body diagram of the vehicle when cruising. The tilt angle β is the angle between the arm and the central body, and the angle of attack α is the angle between the central body and the horizon.

$$f_D = -\frac{1}{2}C_D(\alpha)\rho Av^2x_E \tag{1}$$

$$f_L = \frac{1}{2}C_L(\alpha)\rho Av^2z_E \tag{2}$$

130 Where α is the angle of attack, $C_D(\alpha)$ and $C_L(\alpha)$ are the angle-of-attack-dependent drag and lift
 131 coefficients, ρ is the density of air, v is the speed of the quadcopter, and A is the reference area which

132 is the projection area of the vehicle onto its top surface. Figure 5 shows the breakdown of forces on the
133 quadcopter when it is cruising. The force balance of the quadcopter can be expressed as:

$$f_{\Sigma} \sin(-\alpha + \beta) = \frac{1}{2} C_D(\alpha) \rho A v^2 \quad (3)$$

$$f_{\Sigma} \cos(-\alpha + \beta) = m_{\Sigma} g - \frac{1}{2} C_L(\alpha) \rho A v^2 \quad (4)$$

134 Where $f_{\Sigma} := \sum_{i=1}^4 f_{p_i}$ is the total thrust from all 4 propellers, m_{Σ} is the total mass of the vehicle, and g
135 is the gravitational acceleration. We will use the results here to design for the tilt angle in Section 3.3.

136 2.4 Rigid body dynamics

137 We derive the rigid body dynamics of the vehicle, especially those governing the tilting of the arms. We
138 will use these results in Section 3.1 to design for the vehicle configuration, and in Section 4.1 to compute
139 the bounds on the control to ensure that mid-air morphing happens in a controlled manner. Since tilting
140 and untilting usually happen during the early and late stages of flight where the speed is low, we will
141 not consider aerodynamic forces here. The translational and rotational dynamics of the vehicle can be
142 computed using Newton's and Euler's laws of motion Zipfel (2007). The translational dynamics of the
143 central body expressed in the Earth frame E , and the rotational dynamics of the central body expressed in
144 the central body frame C are:

$$m_C \ddot{\mathbf{d}}_{CE}^E = m_C \mathbf{g}^E + \mathbf{R}^{EC} \sum_{i=1}^4 \left(\mathbf{f}_{r_i}^C + \mathbf{f}_{s_i}^C \right) \quad (5)$$

$$\mathbf{J}_C^C \dot{\boldsymbol{\omega}}_{CE}^C + \mathbf{S} \left(\boldsymbol{\omega}_{CE}^C \right) \mathbf{J}_C^C \boldsymbol{\omega}_{CE}^C = \sum_{i=1}^4 \left(\boldsymbol{\tau}_{r_i}^C + \mathbf{S} \left(\mathbf{d}_{H_i C}^C \right) \mathbf{f}_{r_i}^C + \mathbf{S} \left(\mathbf{d}_{C S_i}^C \right) \mathbf{f}_{s_i}^C \right) \quad (6)$$

145 The translational and rotational dynamics of arm i expressed both in the corresponding arm frame are:

$$\begin{aligned} m_{A_i} \mathbf{R}^{A_i E} \ddot{\mathbf{d}}_{CE}^E &= -m_{A_i} \mathbf{R}^{A_i C} \left(\mathbf{S} \left(\mathbf{d}_{C H_i}^C \right) \dot{\boldsymbol{\omega}}_{CE}^C + \mathbf{S} \left(\boldsymbol{\omega}_{CE}^C \right) \mathbf{d}_{C H_i}^C \boldsymbol{\omega}_{CE}^C \right) \\ &\quad - m_{A_i} \left(\mathbf{S} \left(\mathbf{d}_{H_i A_i}^{A_i} \right) \dot{\boldsymbol{\omega}}_{A_i E}^{A_i} + \mathbf{S} \left(\boldsymbol{\omega}_{A_i E}^{A_i} \right) \mathbf{S} \left(\mathbf{d}_{H_i A_i}^{A_i} \right) \boldsymbol{\omega}_{A_i E}^{A_i} \right) \\ &\quad + \mathbf{z}_{A_i}^{A_i} f_{p_i} - \mathbf{f}_{r_i}^{A_i} - \mathbf{f}_{s_i}^{A_i} + m_{A_i} \mathbf{R}^{A_i E} \mathbf{g}^E \end{aligned} \quad (7)$$

$$\begin{aligned} \mathbf{J}_{A_i}^{A_i} \dot{\boldsymbol{\omega}}_{A_i E}^{A_i} + \mathbf{S} \left(\boldsymbol{\omega}_{A_i E}^{A_i} \right) \mathbf{J}_{A_i}^{A_i} \boldsymbol{\omega}_{A_i E}^{A_i} &= \mathbf{S} \left(\mathbf{d}_{P_i A_i}^{A_i} \right) \mathbf{z}_{A_i}^{A_i} f_{p_i} + \mathbf{z}_{A_i}^{A_i} \boldsymbol{\tau}_{p_i} - \boldsymbol{\tau}_{r_i}^{A_i} - \mathbf{S} \left(\mathbf{d}_{H_i A_i}^{A_i} \right) \mathbf{f}_{r_i}^{A_i} \\ &\quad - \mathbf{S} \left(\mathbf{d}_{M_i A_i}^{A_i} \right) \mathbf{f}_{s_i}^{A_i} - J_{p_i} \mathbf{S} \left(\boldsymbol{\omega}_{A_i E}^{A_i} \right) \boldsymbol{\omega}_{p_i} \mathbf{z}_{A_i}^{A_i} \end{aligned} \quad (8)$$

146 Where J_{p_i} is the moment of inertia of the rotor, $\boldsymbol{\omega}_{p_i}$ is the rotational speed of the propeller, and the last
147 term $J_{p_i} \mathbf{S} \left(\boldsymbol{\omega}_{A_i E}^{A_i} \right) \boldsymbol{\omega}_{p_i} \mathbf{z}_{A_i}^{A_i}$ indicates the gyroscopic torque produced by rotating the spinning rotor.

148 Now we consider the dynamics of the whole quadcopter. Its translational dynamics in the Earth frame E
149 and rotational dynamics in the central body frame C are:

$$m_{\Sigma} \ddot{\mathbf{d}}_{CE}^E = m_{\Sigma} \mathbf{g}^E + \mathbf{R}^{EC} \mathbf{z}_{A_i}^C \sum_{i=1}^4 f_{p_i} = m_{\Sigma} \mathbf{g}^E + \mathbf{R}^{EC} \mathbf{z}_{A_i}^C f_{\Sigma} \quad (9)$$

$$\mathbf{J}_{\Sigma}^C \dot{\boldsymbol{\omega}}_{CE}^C + \mathbf{S}(\boldsymbol{\omega}_{CE}^C) \mathbf{J}_{\Sigma}^C \boldsymbol{\omega}_{CE}^C = \sum_{i=1}^4 \mathbf{S}(\mathbf{d}_{P_i C}^C) \mathbf{z}_{A_i}^C f_{p_i} + \mathbf{z}_{A_i}^C \tau_{p_i} = \boldsymbol{\tau}_{\Sigma}^C \quad (10)$$

150 Where \mathbf{J}_{Σ} is the moment of inertia of the whole quadcopter, and $\boldsymbol{\tau}_{\Sigma}$ is the net torque produced by the 4
151 propellers on the quadcopter. We can use these equations to compute the linear and angular accelerations
152 of the quadcopter:

$$\ddot{\mathbf{d}}_{CE}^E = \mathbf{g}^E + \frac{1}{m_{\Sigma}} \mathbf{R}^{EC} \mathbf{z}_{A_i}^C f_{\Sigma} \quad (11)$$

$$\dot{\boldsymbol{\omega}}_{CE}^C = \mathbf{J}_{\Sigma}^{C-1} \boldsymbol{\tau}_{\Sigma}^C - \mathbf{S}(\boldsymbol{\omega}_{CE}^C) \mathbf{J}_{\Sigma} \boldsymbol{\omega}_{CE}^C \quad (12)$$

153 Finally, plugging these equations back into the dynamics of the arm, we can find the reaction force $\mathbf{f}_{r_i}^{A_i}$
154 and torque $\boldsymbol{\tau}_{r_i}^{A_i}$ acting at the hinge:

$$\begin{aligned} \mathbf{f}_{r_i}^{A_i} = & m_A \left(\mathbf{R}^{A_i E} \left(\mathbf{g}^E - \ddot{\mathbf{d}}_{CE}^E \right) - \mathbf{S}(\mathbf{d}_{C A_i}^{A_i}) \mathbf{R}^{A_i C} \dot{\boldsymbol{\omega}}_{CE}^C \right. \\ & \left. + \mathbf{R}^{A_i C} \left(\mathbf{S}(\boldsymbol{\omega}_{CE}^C) \mathbf{S}(\mathbf{d}_{C H_i}^C) \boldsymbol{\omega}_{CE}^C + \mathbf{S}(\boldsymbol{\omega}_{A_i E}^C) \mathbf{S}(\mathbf{d}_{H_i A_i}^C) \boldsymbol{\omega}_{A_i E}^C \right) \right) + \mathbf{z}_{A_i}^{A_i} f_{p_i} - \mathbf{f}_{s_i}^{A_i} \end{aligned} \quad (13)$$

$$\begin{aligned} \boldsymbol{\tau}_{r_i}^{A_i} = & \mathbf{R}^{A_i C} \boldsymbol{\tau}_{p_i}^C - \mathbf{S}(\mathbf{d}_{M_i A_i}^{A_i}) \mathbf{f}_{s_i}^{A_i} - \mathbf{S}(\mathbf{d}_{H_i A_i}^{A_i}) \mathbf{f}_{r_i}^{A_i} - \mathbf{J}_{A_i}^{A_i} \mathbf{R}^{A_i C} \dot{\boldsymbol{\omega}}_{CE}^C \\ & - \mathbf{R}^{A_i C} \mathbf{S}(\boldsymbol{\omega}_{A_i E}^C) \left(\mathbf{R}^{A_i C} \right)^T \mathbf{J}_{A_i}^{A_i} \mathbf{R}^{A_i C} \boldsymbol{\omega}_{A_i E}^C + J_{p_i} \mathbf{S}(\boldsymbol{\omega}_{A_i E}^{A_i}) \boldsymbol{\omega}_{p_i} \mathbf{z}_{A_i}^{A_i} \end{aligned} \quad (14)$$

155 We note that for the arm to remain untilted, the hinge should only apply a negative reaction torque on the
156 arm. Similarly, for the arm to remain tilted, the hinge should only apply a positive reaction torque on the
157 arm. In math form, $\mathbf{y}_{A_i}^{A_i} \cdot \boldsymbol{\tau}_{r_i}^{A_i} \leq 0$ if the arm is to remain untilted, and $\mathbf{y}_{A_i}^{A_i} \cdot \boldsymbol{\tau}_{r_i}^{A_i} \geq 0$ if the arm is to remain
158 tilted. We note that this constraint only holds when the arms tilt independently. However, the tilting of the
159 arms could be coupled mechanically to relax the bounds. There are three arm coupling configurations. The
160 first is the non-coupled configuration, where each arm tilts separately from one another. The second is the
161 side-coupled configuration, where the two arms at the front are coupled and the two arms at the back are
162 coupled, or the two arms on the left are coupled and the two arms on the right are coupled. The third is
163 the all-coupled configuration, where all four arms are coupled to rotate together. The thrust bounds thus
164 become:

$$\text{Non-coupled : } \mathbf{y}_{A_i}^{A_i} \cdot \boldsymbol{\tau}_{r_i}^{A_i} \leq 0, \text{ for } i \in \{1, 2, 3, 4\} \quad (15)$$

$$\text{Side-coupled : } \begin{cases} \mathbf{y}_{A_1}^{A_1} \cdot \boldsymbol{\tau}_{r_1}^{A_1} + \mathbf{y}_{A_4}^{A_4} \cdot \boldsymbol{\tau}_{r_4}^{A_4} \leq 0 \\ \mathbf{y}_{A_2}^{A_2} \cdot \boldsymbol{\tau}_{r_2}^{A_2} + \mathbf{y}_{A_3}^{A_3} \cdot \boldsymbol{\tau}_{r_3}^{A_3} \leq 0 \end{cases}, \text{ or } \begin{cases} \mathbf{y}_{A_1}^{A_1} \cdot \boldsymbol{\tau}_{r_1}^{A_1} + \mathbf{y}_{A_2}^{A_2} \cdot \boldsymbol{\tau}_{r_2}^{A_2} \leq 0 \\ \mathbf{y}_{A_3}^{A_3} \cdot \boldsymbol{\tau}_{r_3}^{A_3} + \mathbf{y}_{A_4}^{A_4} \cdot \boldsymbol{\tau}_{r_4}^{A_4} \leq 0 \end{cases} \quad (16)$$

$$\text{All-coupled : } \sum_{i=1}^4 \mathbf{y}_{A_i}^{A_i} \cdot \boldsymbol{\tau}_{r_i}^{A_i} \leq 0 \quad (17)$$

165 We will use the results here to evaluate the vehicle agility and choose the arm-coupling configuration in
 166 Section 3.1 and Section 3.2, and compute the bounds on the control inputs to ensure that mid-air morphing
 167 happens in a controlled manner in Section 4.1.

3 DESIGN

168 In this section, we will discuss the design of the quadcopter. The key design parameters are the arm
 169 coupling configuration and the tilt angle. The arm coupling configuration affects vehicle agility. The tilt
 170 angle mainly affects the drag force, flight speed, and high-speed agility. We design our vehicle by first
 171 choosing an arm coupling configuration and designing an overall vehicle frame. Then, we will use the
 172 parameters of the vehicle frame to analyze the impact of the tilt angle on the vehicle performance and
 173 decide on the tilt angle.

174 3.1 Arm-coupling configuration and agility

175 For a conventional quadcopter, the only limits on the vehicle agility are the maximum and minimum
 176 thrusts and torques that a propeller can produce $(f_{min}, f_{max}, \tau_{min}, \tau_{max})$. For our vehicle, however, we
 177 need to impose additional bounds on the propeller thrusts to prevent the arms from tilting and untilting
 178 when not commanded to. These bounds are governed by the spring forces f_{s_i} and some other dynamics
 179 effects as shown in Section 2.4.

180 To get a more intuitive understanding of how these bounds affect the agility of the vehicle and what we
 181 can do about it, let us consider a simplified case where the quadcopter is initially hovering in the untilted
 182 configuration, the angular acceleration is small, and the angular speed is small. $\mathbf{R}^{A_i C}$ thus becomes identity,
 183 and all terms of vehicle angular acceleration and quadratic terms of vehicle angular velocity drop out. The
 184 reaction torque in the $\mathbf{y}_{A_i}^{A_i}$ direction from Equation 14 thus simplifies to:

$$\begin{aligned} \mathbf{y}_{A_i}^{A_i} \cdot \boldsymbol{\tau}_{r_i}^{A_i} &= -\mathbf{y}_{A_i}^{A_i} \cdot \left(\mathbf{S} \left(\mathbf{d}_{M_i A_i}^{A_i} \right) + \mathbf{S} \left(\mathbf{d}_{A_i H_i}^{A_i} \right) \right) \mathbf{f}_{s_i}^{A_i} + d_{H_i A_i, x}^{A_i} \left(-m_A \frac{f_{\Sigma}}{m_{\Sigma}} + f_{p_i} \right) \\ &\quad + \mathbf{y}_{A_i}^{A_i} \cdot \left(J_{p_i} \mathbf{S} \left(\boldsymbol{\omega}_{A_i E}^{A_i} \right) \omega_{p_i} \mathbf{z}_{A_i}^{A_i} \right) \end{aligned} \quad (18)$$

$$= d_{M_i H_i, x}^{A_i} f_{s_i, z}^{A_i} + d_{H_i A_i, x}^{A_i} \left(-m_A \frac{f_{\Sigma}}{m_{\Sigma}} + f_{p_i} \right) - J_{p_i} \omega_{A_i E, x}^{A_i} \omega_{p_i} \quad (19)$$

185 Where $d_{M_i H_i, x}^{A_i} f_{s_i, z}^{A_i}$ represents the torque that the spring applies on the arm in the $\mathbf{y}_{A_i}^{A_i}$ direction around
 186 the hinge, $d_{H_i A_i, x}^{A_i} \left(-m_A \frac{f_\Sigma}{m_\Sigma} + f_{p_i} \right)$ represents the net torque from the thrust of the propeller and the
 187 inertial force from accelerating the arm around the hinge, and $J_{p_i} \omega_{A_i E, x}^{A_i} \omega_{p_i}$ represents the gyroscopic
 188 torque from the rotor. The propeller thrust just enough to tilt the arm is thus:

$$f_{p_i, tilt} = m_A \frac{f_\Sigma}{m_\Sigma} - \frac{d_{M_i H_i, x}^{A_i}}{d_{H_i A_i, x}^{A_i}} f_{s_i, z}^{A_i} + \frac{J_{p_i} \omega_{A_i E, x}^{A_i} \omega_{p_i}}{d_{H_i A_i, x}^{A_i}} \quad (20)$$

189 The tilting behavior is thus determined by not only the spring-related parameters which the designer
 190 can decide, but also the roll motion of the vehicle due to the gyroscopic torque $J_{p_i} \omega_{A_i E, x}^{A_i} \omega_{p_i}$. It turns
 191 out that the gyroscopic torque has a major negative impact on the agility of the vehicle. This is because
 192 the momentum of the rotor $J_{p_i} \omega_{p_i}$ is usually quite large due to the high rotational speed of the rotor, and
 193 its product with the roll speed of the quadcopter which gives the gyroscopic torque could easily exceed
 194 the torque from the spring that is holding the arm in place, which can result in unintended tilting and
 195 untilting. To reduce the impact of the gyroscopic torque on the tilting behavior, we will have to couple the
 196 rotations of two adjacent arms, and force them to tilt together. Since every two adjacent propellers spin in
 197 opposite directions, the net angular momentum will cancel out if the speeds are close, and will significantly
 198 reduce the gyroscopic torque reflected on the arms. The uncoupled configuration of Equation 15 is thus not
 199 physically meaningful for most vehicles, and coupling the arms is always required. Near hover, because all
 200 rotors have similar speeds, coupling the arms essentially makes the gyroscopic torque drop out from the
 201 force balance, which will then further simplify the thrust to tilt the arm to:

$$f_{p_i, tilt} = m_A \frac{4f_{p_i, tilt}}{m_\Sigma} - \frac{d_{M_i H_i, x}^{A_i}}{d_{H_i A_i, x}^{A_i}} f_{s_i, z}^{A_i} \quad (21)$$

202 The tilt thrust is now only related to the mechanical properties of the vehicle, and is thus a design
 203 parameter that we can choose. The same applies to the untilt thrust. Typically, we will want the tilt thrust to
 204 be large but smaller than the propeller's maximum thrust, and the untilt thrust to be small but larger than
 205 the propeller's minimum thrust. This will ensure a wide thrust range in either configuration and improves
 206 the agility of the vehicle. Near hover, the propeller thrust is thus bounded by $\{f_{min}, f_{p_i, tilt}\}$ when the arms
 207 are untilted, and $\{f_{p_i, untilt}, f_{max}\}$ when the arms are tilted. Once the desired tilt and untilt thrusts are set,
 208 the corresponding spring and anchoring points can be picked to generate the desired thrusts.

209 We do note that coupling the arms increases the complexity of the vehicle, as some external connecting
 210 rods may be required. However, we also note that the two arms at the front share the same axis for tilting,
 211 as well as the two arms at the back. Therefore, we can use a single arm to mount the two rotors at the front
 212 and at the back. Then we will only need to use one hinge and one spring to tilt each rotor pair. This will
 213 make the quadcopter H-shaped instead of X-shaped, and will eliminate the need for an external connecting
 214 rod.

215 Figure 6 shows an H-shaped vehicle and an X-shaped vehicle. While using the H-shaped frame increases
 216 the length of the quadcopter's fuselage, having a longer fuselage makes the quadcopter more streamlined

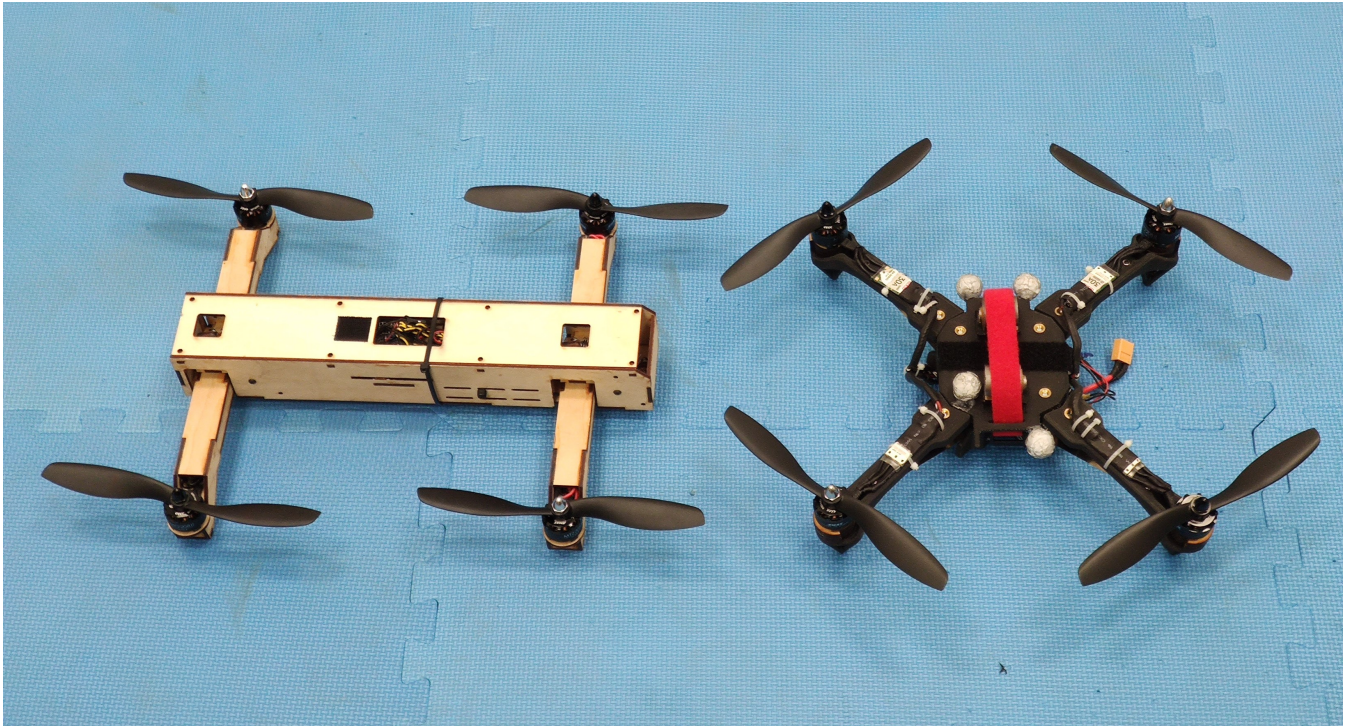


Figure 6. H-shaped (left) vs X-shaped (right) quadcopter frame. Using the H-shaped frame means that a single hinge and a single spring can be used to tilt two propellers at the same time, which reduces the mechanical complexity of the vehicle.

217 and thus more aerodynamically efficient. Considering the agility of the vehicle, it is recommended to use
 218 the side-coupled configuration for slow maneuvers, and use the all-coupled configuration for more agile
 219 maneuvers. An example of how a vehicle with the all-coupled configuration is more agile than a vehicle
 220 with the side-coupled configuration is provided later in Section 4.1. In addition, an H-shaped quadcopter
 221 frame is usually preferred in order to reduce mechanical complexity. Once the arm-coupling configuration
 222 is chosen, the overall vehicle frame can be designed. Next, the relevant parameters can be used to design
 223 for the tilt angle.

224 3.2 Experimental vehicle frame design

225 Following the ideas of Section 3.1, we decided to use the all-coupled configuration for our experimental
 226 vehicle, and developed an H-shaped vehicle frame. The properties of the experimental vehicle frame are
 227 given in Table 1. The overall size of the vehicle is designed to be similar to a commonly used quadcopter.
 228 The motors are the EMAX MT2208 brushless motors, and the propellers are 8' 8045 ABS propellers. Both
 229 are commercially available. In order to avoid discharging the battery at a rate beyond the safety range, we
 230 set our cap on the individual propeller thrust at $f_{max} = 4.5\text{N}$. The drag and lift coefficients are determined
 231 experimentally by flying the vehicle at various constant speeds and curve-fitting the measured lift and drag
 232 forces. The rotations of all four arms are synchronized by using a four-bar mechanism that links the front
 233 arm to the rear arm. The four-bar mechanism can also be removed to convert the vehicle to the side-coupled
 234 configuration. While the mass of the springs can be different depending on the tilt angle, we can reasonably
 235 expect the entire tilting mechanism to add a mass of 50 grams, which is about 6 percent of the mass of the
 236 whole vehicle.

Table 1. Experimental vehicle frame properties.

Symbol	Parameter	Value
m_{A_i}	Individual arm mass	75g
m_C	Central body mass	550g
m_Σ	Total vehicle mass	850g
m_T	Tilting mechanism mass	50g
A	Reference area	0.047m^2
C_D	Fitted drag coefficient equation	$0.773\alpha^2 + 0.543$
C_L	Fitted lift coefficient equation	1.264α
l	Distance between adjacent propellers	27cm
a	Tilt arm length	3cm
$\mathbf{d}_{P_i H_i}^{A_i}$	Position of the propeller with respect to the hinge	$[-a, 0, -1]^T \text{cm}$
$f_{\Sigma, \text{tilt}}$	Total thrust to tilt the propellers at hover	13N
$f_{\Sigma, \text{untilt}}$	Total thrust to untilt the propellers at hover	2.5N
$f_{\Sigma, \text{max}}$	Maximum total thrust	18N
f_{max}	Maximum individual propeller thrust	4.5N
f_{min}	Minimum individual propeller thrust	0N

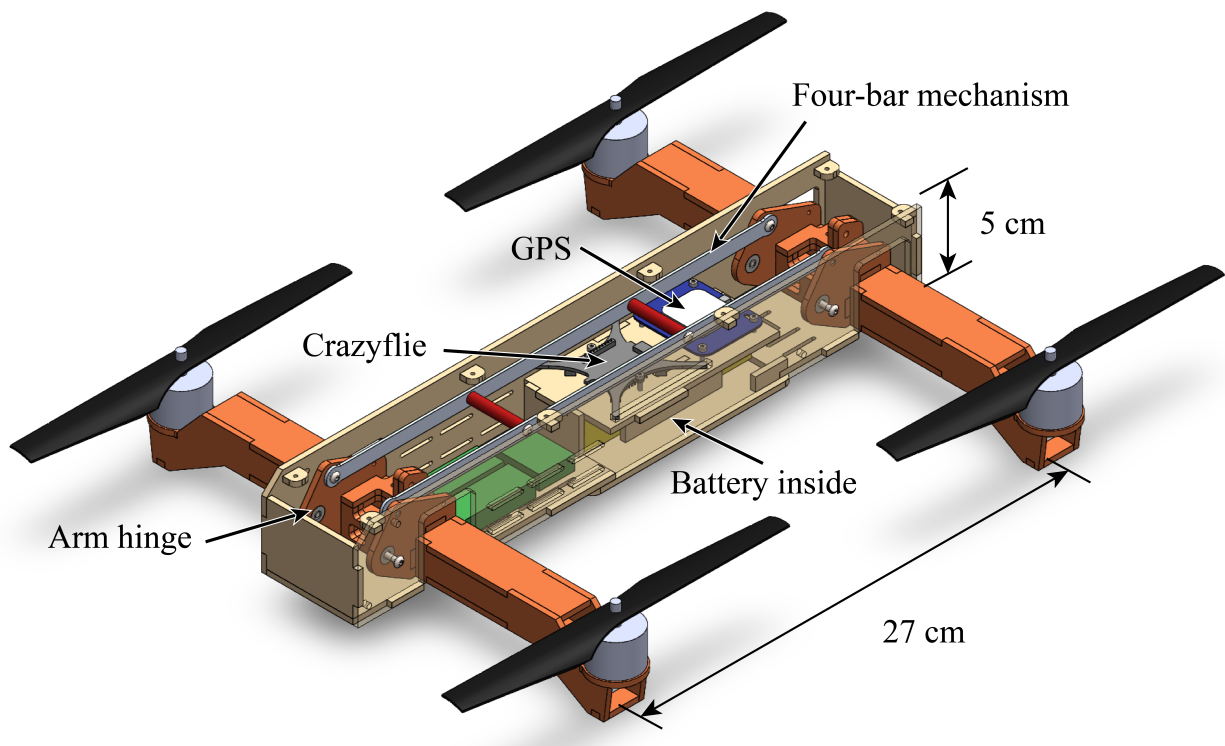


Figure 7. The experimental vehicle frame with the top cover plate taken off. The fuselage shown in beige is constructed with laser-cut wood. The arms shown in red orange are allowed to rotate around the arm hinges, and the rotations of the front and rear arms are coupled by a four-bar mechanism. Round stand-offs shown in red are installed on the long connecting rod of the four-bar mechanism to prevent buckling. Slots are cut on the fuselage for zip-tying wires and other electronics including the ESCs shown in green.

237 Figure 7 shows the experimental vehicle frame with the top cover plate taken off. We used laser-cut
 238 plywood to construct the overall frame because it allows for fast fabrication and provides high-enough
 239 precision. The plywood also shows high strength and rigidity which is desirable for aerial vehicles. The
 240 overall size of the vehicle frame is chosen to match the area span by the four propellers for compactness.

241 3.3 Tilt angle

242 Next, we need to choose a tilt angle. The tilt angle mainly affects 3 vehicle performance indicators,
 243 including the maximum flight speed, high-speed agility, and pitch agility. We will first formulate how we
 244 can compute these vehicle performance indicators using the aerodynamics model from Section 2.3. Then,
 245 we will use the experimental vehicle's frame parameters to evaluate the vehicle performance and decide
 246 the tilt angle and the remaining vehicle parameters in Section 3.4.

247 3.3.1 Maximum cruise speed

248 A regular quadcopter is usually not able to achieve a high top speed because it must tilt its body toward
 249 the forward flight direction, which increases the area subject to air resistance. This further increases the
 250 drag force and requires the propellers to produce even more thrust. However, our proposed vehicle is able
 251 to reduce the tilt angle of the central body and therefore could fly at a higher speed given the same hardware
 252 limit.

253 The relationship between the maximum speed and the corresponding designed tilt angle β can be solved
 254 given the limitation on the vehicle hardware performance. While the vehicle hardware performance can
 255 be limited by a range of factors, including the propeller structural strength, ESC current rating, etc., and
 256 is dependent on the vehicle speed and other external influences, we will assume that all of these can be
 257 generalized to a maximum total thrust of the vehicle $f_{\Sigma, max}$. The correlation between v_{max} and β can be
 258 solved by maximizing v_{max} under the following constraints:

$$\text{Cruise dynamics : } \begin{cases} f_{\Sigma} \sin(-\alpha + \beta) = \frac{1}{2} C_D(\alpha) \rho A v_{max}^2 \\ f_{\Sigma} \cos(-\alpha + \beta) = m_{\Sigma} g - \frac{1}{2} C_L(\alpha) \rho A v_{max}^2 \end{cases} \quad (22)$$

$$\text{Thrust limit : } \begin{cases} f_{\Sigma} \leq f_{\Sigma, max} \end{cases} \quad (23)$$

259 The solution to this problem for our experimental vehicle frame is provided in Section 3.4.

260 3.3.2 High-speed agility

261 When a quadcopter flies at the maximum cruise speed, all of the thrust capacity is used to counter the
 262 vehicle weight and the drag, meaning that it cannot maneuver in any other manner, e.g. accelerate laterally
 263 to avoid an obstacle, without falling and reducing its speed. However, if the propellers are allowed to tilt,
 264 due to the reduction in drag, the vehicle will no longer saturate its thrust at the same cruise speed. This
 265 enables a greater portion of the vehicle's thrust capacity to be used for maneuvering instead of merely
 266 countering drag at high speed, and will improve the high-speed agility of the vehicle. To quantify the agility
 267 of the proposed vehicle, we will consider an obstacle-avoidance example. For analysis, we will consider
 268 the following simplified maneuvers of the vehicle:

269 1. Cruise stage

270 a. Cruises at a maximum constant speed of v_{avoid} in the Earth x-direction \mathbf{x}_E ,

- 271 2. Turning stage
- 272 a. The vehicle detects an obstacle at a distance S in front of it, and starts a turning maneuver,
- 273 b. Constant maximum positive roll torque $\tau_{x,max}$ around the roll axis of the arm frame x_A , and constant
- 274 maximum pitch torque $\tau_{y,max}$ around the pitch axis of the arm frame y_A for time Δt ,
- 275 c. Constant maximum negative roll torque $-\tau_{x,max}$ around the roll axis of the arm frame x_A , and
- 276 constant maximum pitch torque $-\tau_{y,max}$ around the pitch axis of the arm frame y_A for time Δt ,
- 277 3. Lateral acceleration stage
- 278 a. The roll and pitch torques will change the orientation of the vehicle to allow it to accelerate laterally
- 279 in the Earth y -direction to avoid the obstacle, while maintaining the height and x -direction speed of
- 280 the vehicle.
- 281 b. By the time the x -coordinate of the vehicle reaches the obstacle, the vehicle makes a minimum of C
- 282 y -direction clearance with the obstacle.

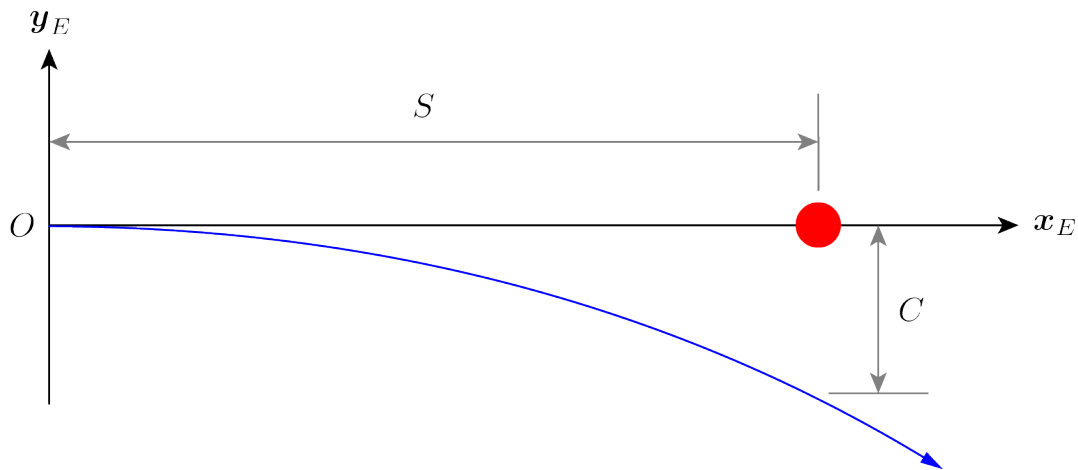


Figure 8. An example obstacle avoidance maneuver. The red dot represents the obstacle and the blue curve represents the flight path. The vehicle is initially flying toward the obstacle and starts an avoidance trajectory at O once it detects the obstacle. By the time the x -position of the vehicle reaches S , it must make a minimum of C y -direction clearance with the obstacle.

283 Figure 8 shows the example obstacle avoidance maneuver. The maximum crash-free cruise speed v_{avoid}

284 thus reflects the high-speed agility of the vehicle. The faster a vehicle can travel without having to crash

285 into the obstacle, the more agile it is. The correlation between v_{avoid} and β can be solved by maximizing

286 v_{avoid} given the following constraints:

$$\text{Cruise dynamics : } \begin{cases} f_{\Sigma,-} \sin(-\alpha_- + \beta) = \frac{1}{2} C_D(\alpha_-) \rho A v_{avoid}^2 \\ f_{\Sigma,-} \cos(-\alpha_- + \beta) = m_{\Sigma} g - \frac{1}{2} C_L(\alpha_-) \rho A v_{avoid}^2 \end{cases} \quad (24)$$

$$\text{Turning dynamics : } \begin{cases} \phi = \frac{\tau_{x,max}}{I_{xx}} \cos \beta \Delta t^2 \\ \psi = -\frac{\tau_{x,max}}{I_{zz}} \sin \beta \Delta t^2 \\ \alpha_+ = \alpha_- - \frac{\tau_{y,max}}{I_{yy}} \Delta t^2 \end{cases} \quad (25)$$

$$\text{Fixed height \& speed : } \begin{cases} f_{\Sigma,+}(\sin(-\alpha_+ + \beta) \cos \phi \cos \psi + \sin \phi \sin \psi) = \frac{1}{2}C_D(\alpha_+)\rho A v_{avoid}^2 \\ f_{\Sigma,+}(\cos(-\alpha_+ + \beta) \cos \phi) = m_{\Sigma}g - \frac{1}{2}C_L(\alpha_+)\rho A v_{avoid}^2 \cos \phi \end{cases} \quad (26)$$

$$\text{Minimum clearance : } \begin{cases} s_y \left(t = \frac{S}{v_{max}} \right) \leq -C \end{cases} \quad (27)$$

$$\text{Torque capacity limit : } \begin{cases} \tau_{y,max} = l\delta(4f_{max} - f_{\Sigma,+}) \cos \beta \\ \tau_{x,max} = l(1 - |\delta|)(4f_{max} - f_{\Sigma,+}) \end{cases} \quad (28)$$

287 Where (ϕ, ψ) are the roll and yaw angles of the vehicle after the turning stage, $(f_{\Sigma,-}, f_{\Sigma,+})$ are the total
 288 vehicle thrusts before and after the turning stage, (α_-, α_+) are the angles of attack before and after the
 289 turning stage, and $\delta \in [0, 1]$ is the fraction of the vehicle's torque capacity used to produce a pitch torque.
 290 Note that although the vehicle produces a roll torque around the roll axis of the arm frame A , the yaw
 291 angle of the vehicle will also change. This is because the tilted propellers will produce a torque around the
 292 yaw axis of the central body frame C . For the given turning maneuver, the total thrust of the vehicle will
 293 monotonically increase from $f_{\Sigma,-}$ at $t = 0$, to $f_{\Sigma,+}$ at $t = 2\Delta t$, and stay at $f_{\Sigma,+}$ for the remainder of the
 294 flight. Throughout the turning stage, since the magnitudes of the desired roll and pitch torques are constant,
 295 the magnitude of the thrust shift across the four propellers to generate the desired roll and pitch torques are
 296 also constant. As a result, at $t = 2\Delta t$ where the total thrust is the highest, the thrust shift will result in one
 297 propeller having the peak thrust. We limit such peak thrust to f_{max} and with some algebraic manipulation,
 298 we can find the torque limit as shown by Equation 28. The solution to this problem is highly dependent on
 299 the vehicle's dynamic properties and is provided for our experimental vehicle frame in Section 3.4.

300 3.3.3 Pitch agility near hover

301 The change in tilt angle β changes the maximum pitch torque τ_y that the vehicle can generate. This is
 302 because when the arms tilt, the moment arm between the front rotors' thrust axes and the rear rotors' thrust
 303 axes changes. Assuming that near hover, the maximum thrust difference between the front rotors and the
 304 rear rotors is Δf , the maximum pitch torque is thus $\tau_{y,max} = \Delta f l \cos \beta$. We note that this torque reduces
 305 as the tilt angle increases. Nevertheless, this problem can be mitigated by designing the rear rotors to be
 306 higher than the front rotors with respect to the central body. For a rotor height offset of Δh , the maximum
 307 pitch torque now becomes $\tau_{y,max} = \Delta f(l \cos \beta + \Delta h \sin \beta)$. However, this results in an increase in vehicle
 308 height, which restricts the vehicle's capability to maneuver in limited space. In addition, the drag area may
 309 also increase if the height offset is achieved by simply skewing the vehicle frame. Therefore, the designer
 310 will need to consider the application to find a balance between maximum pitch torque, the height of the
 311 vehicle, and the other vehicle performance indicators.

312 It is important to note that as the vehicle speed increases, the maximum thrust difference Δf will decrease
 313 due to additional drag on the vehicle. As discussed in the previous section, at high speed, because tilting the
 314 arms reduces the drag, Δf will be relatively larger when the arms are tilted, which can lead to a relatively
 315 higher maximum pitch torque. Therefore, while tilting the arms always reduce the pitch agility of the
 316 vehicle near hover, it does not necessarily reduce the pitch agility at higher speed.

317 3.4 Experimental vehicle tilt angle design

318 Using the parameters of the experimental vehicle frame in Table 1, we can solve for the correlations
 319 between the tilt angle β and the 3 vehicle performance indicators above. For quantifying the high-speed
 320 vehicle agility, we set the detection range to $S = 10\text{m}$ and clearance to $C = 1\text{m}$.

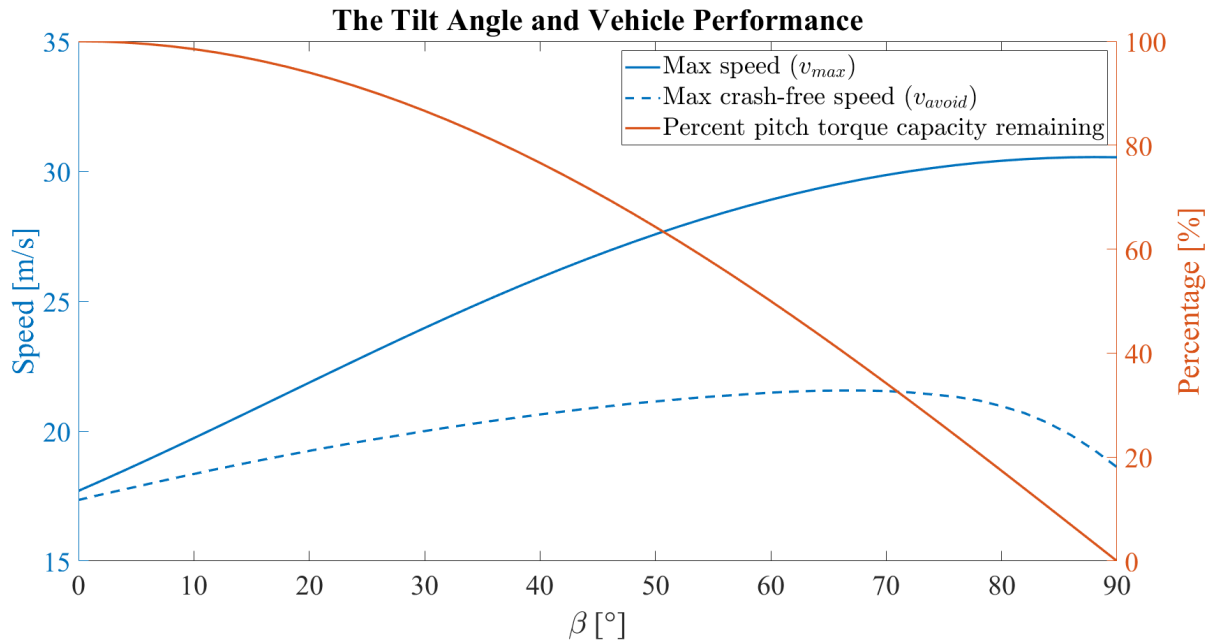


Figure 9. The correlation between the tilt angle and the vehicle performance for the experimental vehicle. Increasing the tilt angle increases the maximum cruise speed of the vehicle with a decreasing marginal gain. Increasing the tilt angle increases the maximum crash-free cruise speed of the vehicle up until $\beta = 68^\circ$. However, increasing the tilt angle decreases the pitch torque capacity.

321 Figure 9 shows how the tilt angle changes the max linear speed v_{max} , the max crash-free speed v_{avoid} ,
 322 and the remaining pitch torque capacity as compared to the torque at zero tilt angle. Increasing the tilt angle
 323 increases the maximum cruise speed of the vehicle with a decreasing marginal gain. The maximum speed
 324 that the vehicle can achieve is 33.28m s^{-1} at a designed tilt angle of 88.2° , which is a 64.8% increase from
 325 the maximum speed of 20.19m s^{-1} when the tilt angle is zero. The maximum crash-free cruise speed of
 326 the vehicle increases as the tilt angle increases, but is maxed out at $\beta = 68^\circ$. The maximum crash-free
 327 cruise speed that the vehicle can achieve is 21.56m s^{-1} at a designed tilt angle of 68° , which is a 24.3%
 328 increase from the maximum speed of 17.35m s^{-1} when the tilt angle is zero. However, increasing the tilt
 329 angle decreases the pitch torque capacity at hover monotonically.

330 In the end, we have chosen a tilt angle of $\beta = 20^\circ$ to preserve much of the pitch torque capacity, while
 331 creating enough differences to be observed in the maximum speed and maximum crash-free speed so
 332 that we can validate the analyses results with experiments. The 20° tilt angle is predicted to increase the
 333 maximum speed of the vehicle from 20.19m s^{-1} to 24.70m s^{-1} , and the maximum crash-free speed of
 334 the vehicle for the given trajectory from 17.35m s^{-1} to 19.24m s^{-1} . On the other side, the reduction in
 335 maximum pitch torque at hover is 6.03% in the tilted configuration.

336 Lastly, we will need to choose the spring and the anchoring points to produce the desired tilt and untilt
 337 thrusts. The spring force, anchoring points, and the desired tilt/untilt thrusts are correlated by Equation
 338 21, and the standard spring equation $\mathbf{f}_{s_i} = -k(\|\mathbf{d}_{S_i M_i}\| - l_0) \frac{\mathbf{d}_{S_i M_i}}{\|\mathbf{d}_{S_i M_i}\|}$. We approach this problem by first
 339 experimentally determining the spring constants for a set of springs in stock that will fit in the vehicle
 340 frame. Then, we compute the exact anchoring points for all the springs by numerically solving the full
 341 equations with additional space constraints. Lastly, we choose the spring and the corresponding anchoring

342 points that would minimize the size of the tilting mechanism. The vehicle's tilt angle and all other relevant
 343 properties are summarized in Table 2.

Table 2. Experimental vehicle tilting-related properties.

Symbol	Parameter	Value
β	Tilt angle	20°
l_0	Spring rest length	1.75cm
k	Spring constant	4N cm^{-1}
$d_{M_i H_i}^{A_i}$	Position of spring end 1 with respect to the hinge	$[-3.5, 0, 1]^T \text{cm}$
$d_{S_i H_i}^{A_i}$	Position of spring end 2 with respect to the hinge	$[1.8, 0, -1.5]^T \text{cm}$

344 To ensure consistent configuration transition in actual flight, it is important to keep the springs under the
 345 limit of proportionality to prevent degradation. For long-term use, fatigue analysis on the springs is desired.
 346 In addition, because the wires powering the rotors will pass around the arm hinges, it is crucial to minimize
 347 the friction that wires introduce to the quadcopter arms by using softer wires, running cables properly, etc.
 348 It is also worth noting that the use of springs is rather a design choice but not the only option. In the end,
 349 our goal is to put a larger torque on the quadcopter arm in the untilted configuration, and a smaller torque
 350 on the quadcopter arm in the tilted configuration. Therefore, other solutions like using magnets of different
 351 strengths to attract the quadcopter arms can be applied, and may even offer a longer life cycle and smaller
 352 size.

353 With the design of the experimental vehicle finalized, we will now validate its capabilities with
 354 experiments.

4 EXPERIMENTAL VALIDATION

355 In this section, we will use the experimental vehicle to validate the capabilities of the proposed design,
 356 including 1. the reliability of the tilting mechanism, 2. the improvement in the top linear speed, 3. the
 357 improvement in the high-speed agility, and 4. the increase in the energy efficiency.

358 4.1 Experiment setup

359 For all of our tests, we fly the vehicle outdoors in a flat grass field at the Richmond Field Station,
 360 Richmond, and localize it by fusing readings from the following sensors:

- 361 1. Inertial measurement unit (accelerometer and rate-gyroscope) running at 500 Hz,
- 362 2. 3-axis magnetometer running at 100 Hz,
- 363 3. Global positioning system running at 5 Hz.

364 The sensor readings are fused via an off-the-shelf extended Kalman filter (EKF) algorithm taken from
 365 the open-source PX4 firmware (Meier et al., 2015). The IMU and magnetometer are a part of the flight
 366 controller and the GPS is connected to the flight controller via a serial port (UART). The EKF is run on
 367 the flight controller at 500 Hz, predicting the states forward using the IMU data, and using the GPS and
 368 magnetometer readings for the correction step of the EKF. The state estimates are then used by the flight
 369 controller for closed-loop control.

370 Data from the above sensors and the state estimates are logged via radio at 100 Hz for post-processing.
 371 Additionally, the voltage and current readings from the battery are measured using a power module and are
 372 also logged to calculate the power consumption of the quadcopter in the untilted and tilted configurations.

373 The quadcopter is controlled autonomously and tracks the desired position, velocity, acceleration, and
 374 yaw angle by using a cascaded position and attitude controller as shown in Figure 10.

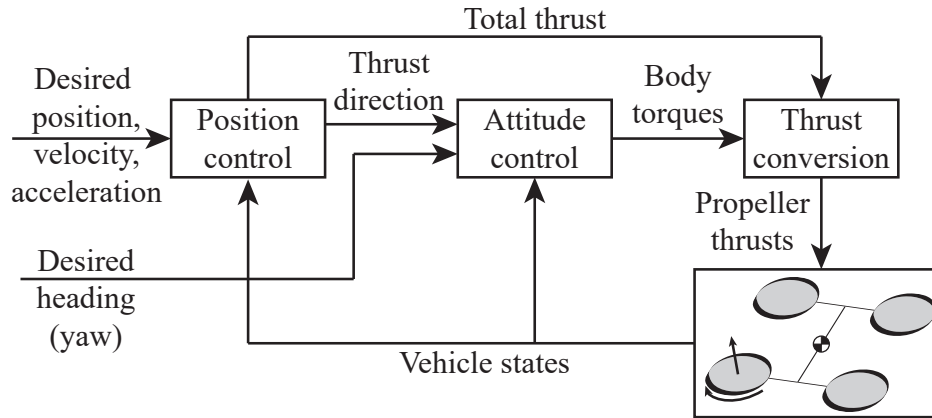


Figure 10. Block diagram of the quadcopter controller.

375 The position and attitude controller computes the desired body torques $\tau^A = [\tau_x, \tau_y, \tau_z]^T$ and total thrust
 376 f_Σ in the combined arm A frame required to track the desired thrust direction and the desired yaw angle.
 377 Individual rotor thrusts $\mathbf{u} = [f_{p1}, f_{p2}, f_{p3}, f_{p4}]^T$ required to generate the desired total thrust and the desired
 378 body torques are then computed using the following mapping:

$$\mathbf{u} = \begin{bmatrix} f_{p1} \\ f_{p2} \\ f_{p3} \\ f_{p4} \end{bmatrix} = \begin{bmatrix} \mathbf{M}_{f_\Sigma} \\ \mathbf{M}_{\tau^A} \end{bmatrix}^{-1} \begin{bmatrix} f_\Sigma \\ \tau_x \\ \tau_y \\ \tau_z \end{bmatrix} = \mathbf{M}^{-1} \begin{bmatrix} f_\Sigma \\ \tau^A \end{bmatrix} \quad (29)$$

379 Where $\mathbf{M}_{f_\Sigma} \in \mathbb{R}^{1 \times 4}$ is the mapping from \mathbf{u} to f_Σ , $\mathbf{M}_{\tau^A} \in \mathbb{R}^{3 \times 4}$ is the mapping from \mathbf{u} to τ^A , and
 380 $\mathbf{M} \in \mathbb{R}^{4 \times 4}$ is the combined mapping. The mapping is computed using the geometry of the vehicle and
 381 the torque τ_{p_i} from each propeller which correlates to the thrust f_{p_i} by $\tau_{p_i} = (-1)^i \kappa f_{p_i}$, where κ is the
 382 thrust to torque coefficient of the propeller. Since the body torques and the desired total thrust are in the
 383 combined arm frame A , the entries for the mapping matrices are given as:

$$\mathbf{M}_{f_\Sigma} = \begin{bmatrix} 1 & 1 & 1 & 1 \end{bmatrix} \quad (30)$$

$$\mathbf{M}_{\tau^A}[:, i] = \mathbf{S} \left(\mathbf{R}^{AC} \mathbf{d}_{P_i C}^C \right) \mathbf{z}_A^A + (-1)^i \kappa \mathbf{z}_A^A \quad (31)$$

384 Lastly, we can compute the combined mapping matrix \mathbf{M} for the untilted and tilted configurations:

$$M_{untilted} = \begin{bmatrix} 1 & 1 & 1 & 1 \\ -\frac{l}{2} & -\frac{l}{2} & \frac{l}{2} & \frac{l}{2} \\ -\frac{l}{2} & \frac{l}{2} & \frac{l}{2} & -\frac{l}{2} \\ -\kappa & \kappa & -\kappa & \kappa \end{bmatrix} \tag{32}$$

$$M_{tilted} = \begin{bmatrix} 1 & 1 & 1 & 1 \\ -\frac{l}{2} & -\frac{l}{2} & \frac{l}{2} & \frac{l}{2} \\ -\cos \beta(a + \frac{l}{2}) + a & \cos \beta(a - \frac{l}{2}) + a & \cos \beta(a - \frac{l}{2}) + a & -\cos \beta(a + \frac{l}{2}) + a \\ -\kappa & \kappa & -\kappa & \kappa \end{bmatrix} \tag{33}$$

385 Combining this with the thrust bounds we computed in Section 2.4, we can find the limit on the total
 386 thrust and the desired body torques. The vehicle in the all-coupled configuration has the highest agility.
 387 The pitch torque capacity is higher, and the thrust bounds are almost not affected by the motion of the
 388 vehicle. The vehicle in the side-coupled has a lower maximum roll and yaw torque when the rolling speed
 389 is high. As an example, Figure 11 shows the limit on the roll torque and the total thrust that the vehicle can
 390 produce in the side-couple and all-coupled configurations for different rolling speeds, to prevent the arms
 391 from untilting in the tilted configuration.

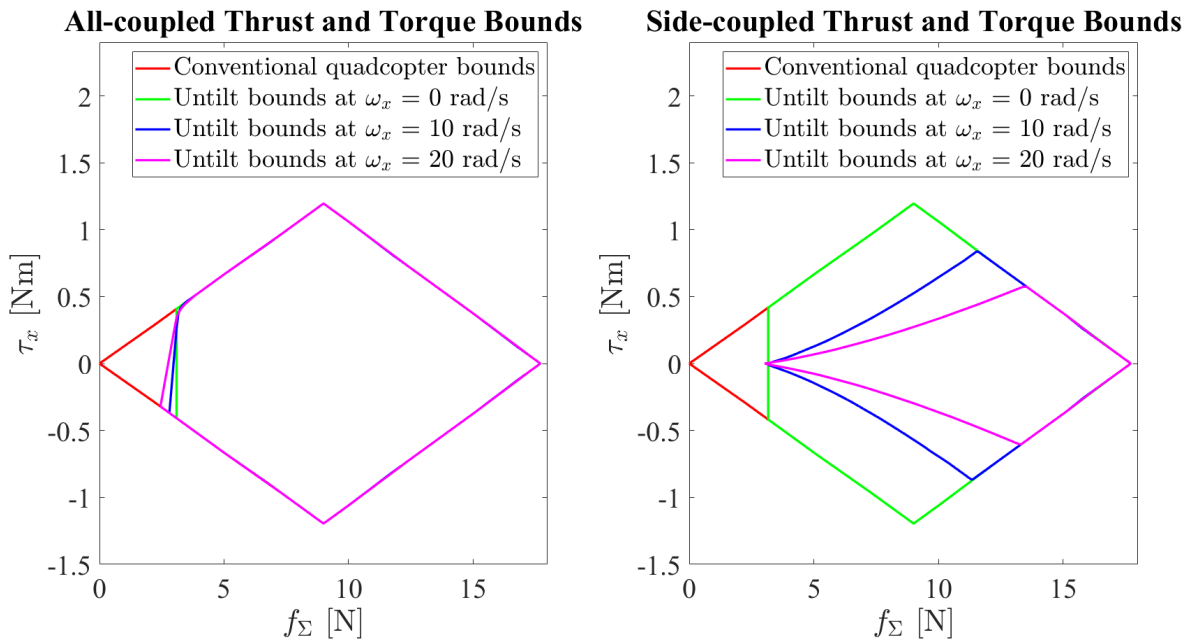


Figure 11. The limit on the roll torque and the total thrust that the vehicle can produce in the side-couple and all-coupled configurations for different rolling speeds, to prevent the arms from untilting in the tilted configuration.

392 As compared to a conventional quadcopter with the same vehicle parameters without the ability to tilt,
 393 the tilt-rotor has tighter bounds on the torque thrust and roll torque to prevent untilting. At zero rolling
 394 speed, the untillt bounds are identical for the all-coupled and side-coupled configurations. As the rolling

395 speed increases, the gyroscopic torque discussed in Section 3.1 comes into play, and tightens the bounds
 396 for the vehicle in the side-coupled configuration. However, in the all-coupled configuration, the bounds are
 397 effectively not affected at all, and the vehicle maintains the same agility regardless of the maneuver. As a
 398 result, we have kept our vehicle in the all-coupled configuration, and we have found that the vehicle is able
 399 to maintain its configuration without any programmed tilt/untilt thrust and torque bounds.

400 4.2 Experiments

401 4.2.1 Changing configuration test

402 The transition between the tilted and untilted configurations is tested. The transition from the untilted
 403 configuration to the tilted configuration is accomplished by commanding a high total thrust for a fraction of
 404 a second. Right after the morphing, the same controller before the transition resumes to function but is
 405 updated to use the tilted mapping matrix M_{tilted} . To accommodate for the change in the vehicle position
 406 from suddenly producing a high thrust, we add an offset to the desired position right after the morphing.
 407 Figure 12 shows the vehicle switching from the untilted to the tilted configuration.



Figure 12. The vehicle switches from the untilted to the tilted configuration. An offset is added to the desired position to accommodate for the change in the vehicle position due to the sudden high thrust.

408 To switch back to the untilted configuration, we simply command a near zero thrust for a fraction of
 409 a second. Right after the morphing, the controller is switched back to use the untilted mapping matrix
 410 $M_{untilted}$. The sudden loss of thrust causes the vehicle to fall, so an opposite offset is added to the desired
 411 position to accommodate for the change in the vehicle position. The tilting and untilting are repeated 20
 412 times and show no signs of failure. Figure 13 shows the vehicle commanded thrust and the measured
 413 accelerations for one tilt and untilt cycle.

414 4.2.2 Maximum linear speed tests

415 The maximum speed of the vehicle is tested by flying the vehicle in a straight line in the following
 416 manner:

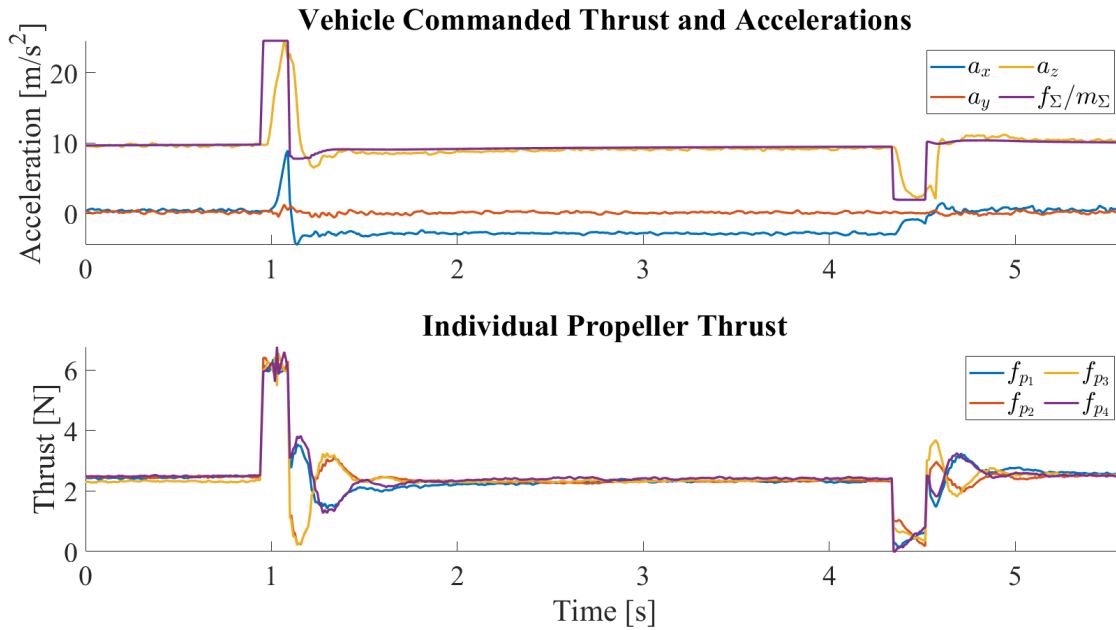


Figure 13. The vehicle commanded thrust normalized by the vehicle mass and the measured accelerations in the central body frame C for one tilt and untilt cycle. At around $t = 1\text{ s}$, the vehicle is commanded to tilt by producing a sudden high thrust. The surge in thrust is followed by a surge in the acceleration along z_C , which is then followed by an increase in the acceleration along x_C , meaning that the thrust axes of the propellers have been tilted forward. The negative x_C acceleration between transitions indicates the change of the vehicle's pitch angle such that the propellers are pointing upward to keep the vehicle at hover. At around $t = 4.5\text{ s}$, the vehicle is commanded to untilt by producing a sudden low thrust. The drop in thrust is followed by a drop in the acceleration along z_C , which is then followed by a drop in the magnitude of acceleration along x_C , meaning that the thrust axes of the propellers have been restored. Despite the change in the mapping matrix, we can see that the individual propeller thrusts are very close once the vehicle has stabilized after the transition.

- 417 1. Accelerate at a constant linear acceleration of a ,
 418 2. Check if the maximum total thrust $f_{\Sigma,max}$ is reached, if so start decelerating until rest.
 419 3. Record the maximum speed that the vehicle has reached v_{max} .

420 Since the maximum total thrust $f_{\Sigma,max}$ is above the tilt thrust $f_{\Sigma,tilt}$, we bolted the tilting mechanism
 421 in the untilted configuration to imitate a vehicle without the ability to tilt. In order to prevent the vehicle
 422 from flying beyond the flight space, we choose a to be 3.125 m s^{-2} . Adding the acceleration term to
 423 Equation 22, we can predict that the maximum speed in the untilted configuration is 17.70 m s^{-1} , and the
 424 maximum speed in the tilted configuration is 21.86 m s^{-1} . The actual experiment is repeated 3 times for
 425 each configuration. The experimental results are summarized in Table 3.

426 We can see that the average maximum speed of the vehicle in the tilted configuration is 12.5% higher
 427 than in the untilted configuration, and the results are repeatable. We do note that the vehicle in the untilted
 428 configuration is flying faster than the prediction. We suspect that this has to do with the fact that the lift
 429 model assumes that the angle of attack is in the linear region which will show a very high downward lift on
 430 the vehicle when the angle of attack is large. However, at this speed, we record that the angle of attack of
 431 the vehicle in the untilted configuration is almost -45° , which is beyond the linear region. As a result, the
 432 actual downward lift on the vehicle is smaller than the prediction, meaning that more of the vehicle thrust
 433 can be used to counteract the drag, thus allowing the vehicle in the untilted configuration to fly faster.

Table 3. Maximum linear speed achieved by the vehicle and the associated angle of attack.

Trial	Untilted		Tilted	
	Max speed	Max angle of attack	Max speed	Max angle of attack
1	18.65m s ⁻¹	-41.47°	20.81m s ⁻¹	-25.79°
2	18.64m s ⁻¹	-45.20°	21.59m s ⁻¹	-16.05°
3	19.05m s ⁻¹	-39.73°	21.02m s ⁻¹	-26.59°
Average	18.77m s ⁻¹	-42.13°	21.14m s ⁻¹	-22.81°
Standard deviation	0.24m s ⁻¹	2.79°	0.40m s ⁻¹	5.87°

434 4.2.3 Obstacle avoidance tests

435 The high-speed agility of the vehicle is tested by having the vehicle track the obstacle avoidance trajectory
 436 discussed in Section 3.3.2. We create an imaginary obstacle on our path with $S = 10\text{m}$, and command the
 437 vehicle to cruise at the computed v_{max} and then turn to avoid the obstacle to achieve a clearance of $C = 1\text{m}$.
 438 We limit the individual propeller thrust at f_{max} , and compare the actual flight speed and clearance with the
 439 commanded ones to evaluate the real agility of the vehicle. The experimental results are summarized in
 440 Table 4.

Table 4. The actual flight speed and clearance and the commanded flight speed and clearance.

Configuration	Commanded speed	Actual speed	Commanded clearance	Actual clearance
Untilted	17.35m s ⁻¹	17.70m s ⁻¹	1m	1.03m
Tilted	19.24m s ⁻¹	19.03m s ⁻¹	1m	1.24m

441 We can see that given the same thrust constraint, the vehicle is able to achieve the commanded clearance
 442 of $C = 1\text{m}$ in both the untilted and tilted configurations, and can reach a higher flight speed without
 443 crashing in the tilted configuration.

444 4.2.4 Aerodynamic performance tests

445 The reduction in drag allows less thrust to be produced to travel at the same speed, which increases the
 446 energy efficiency of the vehicle. To test the aerodynamic performance, the vehicle is flown at commanded
 447 horizontal speeds v_{des} of $\{10.0, 12.5, 15.0, 17.5, 20.0\}\text{m s}^{-1}$ in a straight line in the following manner:

- 448 1. Accelerate from rest to the cruising speed v_{des} over a specified acceleration distance s_{accel} ,
- 449 2. Cruise at v_{des} over a specified cruise distance s_{cruise} ,
- 450 3. Decelerate from cruising speed to rest over a specified deceleration distance s_{decel} .

451 Voltage and current data collected from the power module is evaluated over the steady state of the cruising
 452 portion of the trajectory, which is selected to last five seconds to get approximately 500 data points.

453 A sample plot of power and speed vs. time is shown in Figure 14a. This specific plot is for the case of the
 454 quadcopter commanded to fly in the tilted configuration at 20 m s^{-1} .

455 The plot of average power vs. average speed is shown in Figure 14b. The power consumption is lower
 456 in the tilted configuration than in the untilted configuration at high speed. We can see that the power
 457 consumption in the tilted configuration in the speed range of $15 - 20\text{ m s}^{-1}$ is more than 20% lower as
 458 compared to the untilted configuration.

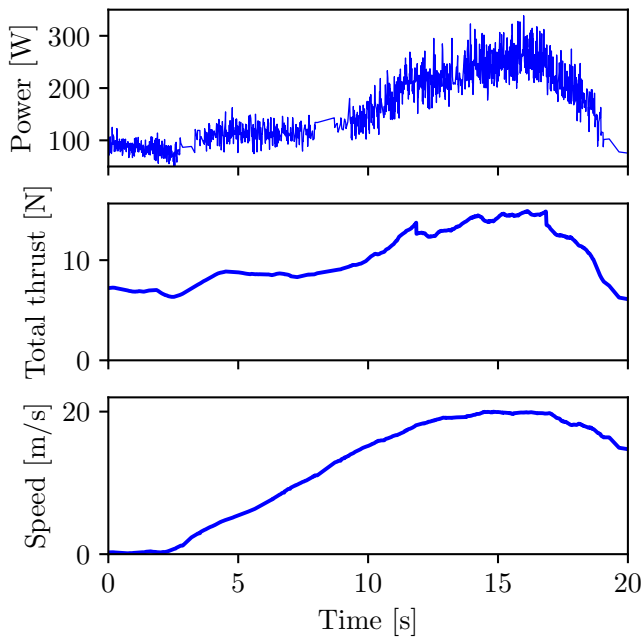


Figure 14a. Power, total thrust, and speed vs. time for a single experiment. Data in this plot is from the experiment where the quadcopter is commanded to fly in the tilted configuration at 20 m s^{-1} .

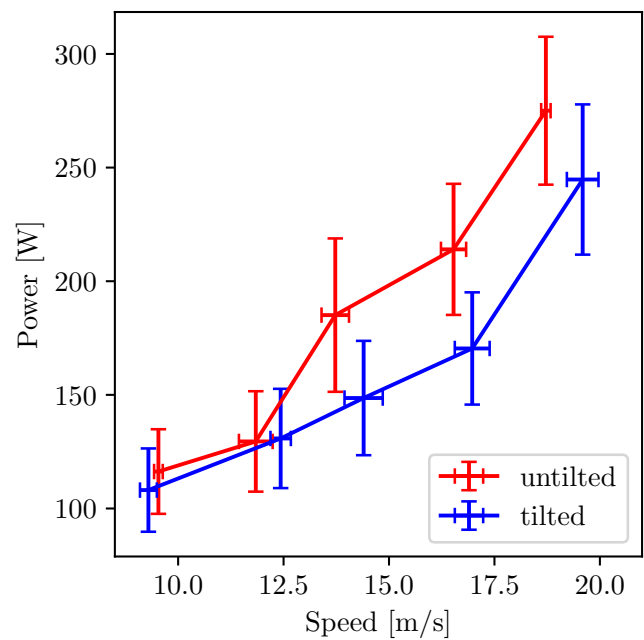


Figure 14b. Power consumption vs. speed when flying in untitled and tilted configurations. The data points are the average values and the error bars represent one standard deviation in the data.

5 CONCLUSION

459 In this paper, we have presented a novel quadcopter design capable of tilting the propellers into the forward
 460 flight direction in mid-air to reduce the drag without the use of additional actuators. The reduction in drag
 461 allows the vehicle to fly at a higher top speed with higher agility, and improves the flight efficiency at
 462 high speed. Unlike the other multirotor–fixed-wing combo quadcopters, the proposed vehicle does not
 463 have wings. While this sacrifices the cruise efficiency, the vehicle has higher agility as the area subject to
 464 aerodynamic forces is kept small. Especially, the vehicle will not have high drag during rolling motion
 465 due to large wings paddling in the air like fixed-wing vehicles. By using simple sprung hinges instead of
 466 actuators or other complex mechanisms, the design is thus relatively less complicated than other aerial
 467 morphing vehicles. On the other side, the use of a passive tilting mechanism means that the arms can only
 468 be tilted in one direction with a fixed tilting angle, and cannot achieve the arbitrary attitude of other actively
 469 tilted quadcopters.

470 The dynamics of such a vehicle were derived. Based on the dynamics, we discussed the key design
 471 parameters including the tilt angle and the vehicle configuration. The effects that these parameters have on
 472 the vehicle performance are presented, and the relevant design trade-offs are discussed. Analyses show
 473 that while the vehicle is always less agile near hover as compared to a conventional vehicle due to the
 474 introduction of additional thrust bounds, it does have a higher top speed and higher agility at high speed as
 475 lesser thrust capacity is used to counteract the aerodynamic forces in the tilted configuration.

476 An experimental vehicle with an overall size similar to a regular quadcopter is built to validate the
 477 analyses. Experiments are done to validate the capabilities of the vehicle. First, the vehicle is shown to
 478 transition between the tilted and untitled configurations reliably. Then, the vehicle is shown to have reached
 479 a higher maximum linear speed under the same thrust limit in the tilted configuration. Furthermore, the

480 vehicle is shown to be more agile at high speed, as it can fly faster while avoiding a defined obstacle in the
481 tilted configuration. Finally, the vehicle is shown to have a better energy efficiency than a conventional
482 quadcopter at a higher speed.

483 The proposed design is thus able to fly at a higher top speed (by 12.5%), has higher high-speed agility
484 (by 7.5%) and higher efficiency (20% lower power consumption for a speed range of 15-20m s⁻¹) with
485 little trade-offs in mechanical complexity and low-speed agility. This can be useful for applications that are
486 time-sensitive, such as package delivery and drone racing. In the future, the vehicle can be designed such
487 that the tilt angle can be easily reconfigured, allowing it to fit a wide range of applications. The frame of the
488 vehicle can also be designed to be more aerodynamically efficient, allowing for an even higher top speed
489 and better high-speed agility. One approach to improve the aerodynamic efficiency of the vehicle frame
490 is to reduce its vertical dimension, which can be achieved by reducing the size of the tilting mechanism
491 through the use of shorter but stronger springs. In addition, the vehicle frame can be designed like an airfoil
492 shape to reduce the drag coefficient, and even generate lift to counteract the vehicle weight.

6 ACKNOWLEDGMENT

493 We gratefully acknowledge financial support from Hong Kong Centre for Logistics Robotics (HKCLR).

494 The experimental testbed at the HiPeRLab is the result of the contributions of many people, a full list of
495 which can be found at <https://hiperlab.berkeley.edu/members/>.

REFERENCES

- 496 Allenspach, M., Bodie, K., Brunner, M., Rinsoz, L., Taylor, Z., Kamel, M., et al. (2020). Design and
497 optimal control of a tiltrotor micro-aerial vehicle for efficient omnidirectional flight. *The International*
498 *Journal of Robotics Research* 39, 1305–1325. doi:10.1177/0278364920943654
- 499 Anderson, R. B., Marshall, J. A., and L'Afflitto, A. (2021). Constrained robust model reference adaptive
500 control of a tilt-rotor quadcopter pulling an unmodeled cart. *IEEE Transactions on Aerospace and*
501 *Electronic Systems* 57, 39–54. doi:10.1109/TAES.2020.3008575
- 502 Bucki, N. and Mueller, M. W. (2019). Design and control of a passively morphing quadcopter. In *2019*
503 *International Conference on Robotics and Automation (ICRA)*. 9116–9122. doi:10.1109/ICRA.2019.
504 8794373
- 505 Erdelj, M., Natalizio, E., Chowdhury, K. R., and Akyildiz, I. F. (2017). Help from the sky: Leveraging
506 UAVs for disaster management. *IEEE Pervasive Computing* 16, 24–32
- 507 Frachtenberg, E. (2019). Practical drone delivery. *Computer* 52, 53–57. doi:10.1109/MC.2019.2942290
- 508 Jaimes, A., Kota, S., and Gomez, J. (2008). An approach to surveillance an area using swarm of fixed wing
509 and quad-rotor unmanned aerial vehicles UAV(s). In *2008 IEEE International Conference on System of*
510 *Systems Engineering (IEEE)*, 1–6
- 511 Jain, K. P., Park, M., and Mueller, M. W. (2020a). Docking two multirotors in midair using relative vision
512 measurements. *arXiv preprint arXiv:2011.05565*
- 513 Jain, K. P., Tang, J., Sreenath, K., and Mueller, M. W. (2020b). Staging energy sources to extend flight
514 time of a multirotor uav. In *2020 IEEE/RSJ International Conference on Intelligent Robots and Systems*
515 *(IROS) (IEEE)*, 1132–1139
- 516 Lin, Q., Cai, Z., Yang, J., Sang, Y., and Wang, Y. (2014). Trajectory tracking control for hovering and
517 acceleration maneuver of quad tilt rotor uav. In *Proceedings of the 33rd Chinese Control Conference*.
518 2052–2057. doi:10.1109/ChiCC.2014.6896946

- 519 Meier, L., Honegger, D., and Pollefeys, M. (2015). Px4: A node-based multithreaded open source robotics
520 framework for deeply embedded platforms. In *2015 IEEE international conference on robotics and*
521 *automation (ICRA)* (IEEE), 6235–6240
- 522 Mueller, M. W., Lee, S. J., and D’Andrea, R. (2022). Design and control of drones. *Annual Review of*
523 *Control, Robotics, and Autonomous Systems* 5, 161–177. doi:10.1146/annurev-control-042920-012045
- 524 Nemati, A., Soni, N., Sarim, M., and Kumar, M. (2016). Design, fabrication and control of a tilt rotor
525 quadcopter:. doi:10.1115/DSCC2016-9929
- 526 Papachristos, C., Alexis, K., and Tzes, A. (2013). Hybrid model predictive flight mode conversion control
527 of unmanned quad-tiltrotors. In *2013 European Control Conference (ECC)*. 1793–1798. doi:10.23919/
528 ECC.2013.6669816
- 529 Poikonen, S. and Campbell, J. (2020). Future directions in drone routing research. *Networks* 77. doi:10.
530 1002/net.21982
- 531 Reinhardt, K. C., Lamp, T. R., Geis, J. W., and Colozza, A. J. (1996). Solar-powered unmanned aerial
532 vehicles. In *IECEC 96. Proceedings of the 31st Intersociety Energy Conversion Engineering Conference*
533 (IEEE), vol. 1, 41–46
- 534 Siebert, S. and Teizer, J. (2014). Mobile 3D mapping for surveying earthwork projects using an unmanned
535 aerial vehicle (UAV) system. *Automation in construction* 41, 1–14
- 536 Thiels, C. A., Aho, J. M., Zietlow, S. P., and Jenkins, D. H. (2015). Use of unmanned aerial vehicles for
537 medical product transport. *Air medical journal* 34, 104–108
- 538 Wu, X., Zeng, J., Tagliabue, A., and Mueller, M. W. (2022). Model-free online motion adaptation for
539 energy-efficient flight of multicopters. *IEEE Access*
- 540 Zipfel, P. H. (2007). *Modeling and Simulation of Aerospace Vehicle Dynamics, 2nd ed* (Reston, VA:
541 American Institute of Aeronautics and Astronautics)